PAPER

Check for updates

Green light-responsive photoelectrochemical sensing nanoplatform based on copper cobaltite nanorods for ultrasensitive detection of furazolidone antibiotic residue in food samples†

Nguyen Ngoc Huyen, [ID] *[a] Xuan-Dinh Ngo, [ID] [a] Vu Thi Huong Mai,[a] Phung Thi Lan Huong,[a] Pham Duc Thang[b] and Le-Anh Tuan [ID] *[ac]

In this research, the preparation of copper cobaltite ($CuCo_2O_4$) nanorods and its potential application in photoelectrochemical sensing platform towards ultrasensitive detection of furazolidone are reported. X-ray diffraction, Raman spectra, scanning electron microscopy, and UV–visible spectroscopy have been performed to confirm the formation, morphology, phase composition, and optical properties of $CuCo_2O_4$ synthesized by a microwave-assisted hydrothermal method. The electrochemical characteristic parameters were calculated *via* electrochemical impedance spectroscopy, cyclic voltammetry, differential pulse voltammetry, and chronoamperometry techniques in the absence and presence of laser light irradiation. The $CuCo_2O_4$-based photoelectrochemical sensing platform with laser light irradiation exhibited outstanding electrochemical performance compared to without laser light irradiation with sensitivity for furazolidone detection of 1.11 μA μM^{-1} cm^{-2} within the linear ranges of 0.25 to 200 μM, and detection limit of 0.03 μM, due to $CuCo_2O_4$ nanorods having a narrow energy gap, a low recombination ratio of electron–hole pairs, and multiple valence states (Co^{2+}/Co^{3+} and Cu^{2+}/Cu^{3+}) structure. In addition, the proposed $CuCo_2O_4$-based photoelectrochemical sensor with light assistance showed good repeatability, anti-interfering capability, long-term stability, and real applicability in honey and milk samples.

1. Introduction

Furazolidone (FZD) is a synthetic nitrofuran antimicrobial drug extensively utilized in veterinary medicine to prevent and treat bacterial infections in livestock and aquaculture, with the objective of improving feed conversion rates and facilitating animal growth.[1,2] Nonetheless, the application of FZD in food-producing animals has been banned in numerous nations due to concerns about its potential to cause adverse health effects in humans, including cancer and genetic mutations, respectively.[3] The overuse of antimicrobial agents not only results in accumulation in the tissues and organs of animals, as well as integration into the food chain in daily life, but also presents environmental risks across multiple matrices, including soil, water, and sediment.[4] Namely, the persistence of

FZD residues in humans may have immunopathological effects, including autoimmunity and carcinogenicity. Besides, it may possess mutagenic qualities and can induce toxicity in the kidneys, bone marrow, and liver.[5] The European Union (EU) and the World Health Organization (WHO) have declared that FZD has no Maximum Residue Limit (MRL), which means that its use in animals raised for food production is prohibited.[6,7] Therefore, to protect public health, it is essential to monitor and manage FZD antibiotic residue in food sectors.

Several traditional methods, including liquid chromatography-tandem mass spectrometry (LC-MS/MS),[8] post-chemiluminescence,[9] high-performance liquid chromatography (HPLC),[10] and enzyme-linked immunosorbent assay (ELISA)[11] have been widely used for FZD detection and monitoring. Nevertheless, these reported methods have some limitations, including (i) time-consuming procedures, (ii) the requirement for high-cost and large-scale equipment, (iii) drawn-out processes, and (iv) difficult sample preparation. In recent years, the electrochemical sensor has emerged as a promising candidate with some outstanding advantages, such as high sensitivity, rapid responsiveness, user-friendly operation, cost-effectiveness, and adaptability for miniaturization. This makes them a preferred option for quantifying different environmental and biological target analytes.[7,12–14] For the development of advanced

[a]*Phenikaa University Nano Institute (PHENA), PHENIKAA University, Hanoi, 12116, Vietnam. E-mail: huyen.nguyenngoc@phenikaa-uni.edu.vn; tuan.leanh@phenikaa-uni.edu.vn*

[b]*Faculty of Physics, VNU Hanoi University of Science, Vietnam National University, Hanoi, 11416, Vietnam*

[c]*Faculty of Materials Science and Engineering, PHENIKAA University, Hanoi, 12116, Vietnam*

electrochemical sensors, the most important factor in enhancing electrochemical signals is the modification of the working electrode surfaces by utilizing different functional nanomaterials.[15,16] Recently, several binary transition metal oxides and mixed metal oxides have been investigated for developing advanced electrochemical sensors.[6,17] The cobaltates (MCo_2O_4) with various coordinated multimetal cations have become a hopeful candidate for the fabrication of electrochemical sensors due to their low toxicity, higher conductivity, cost-effectiveness, rich surface chemistry, and superior redox properties.[13,18–20] Among them, one spinel cobaltates oxide that has garnered interest is copper cobaltite ($CuCo_2O_4$). It has a low band gap (1.6–1.8 eV) and shows promise for energy, photoelectrical, catalytic, and electrochemical applications.[21–25] In contrast to a single metallic oxide, the simultaneous engagement of both redox couples, Co^{3+}/Co^{2+} and Cu^{2+}/Cu^{3+}, improved the redox processes, potentially increasing the photocatalytic activity. In the meantime, the high conductivity of $CuCo_2O_4$, because of the comparatively low activation energy of electron transfer between the cations, improves the pace of electron transfer and the effectiveness of charge separation.[23,25] In addition, the use of light has assisted in the development of a photoelectrochemical sensor platform that has attracted much attention in the analytical technique field and biomarker assays due to its high sensitivity, simplicity, and cost-effectiveness.[26,27] Nevertheless, to the best of our knowledge, the utilization of $CuCo_2O_4$ in photoelectrochemical sensor has not been investigated for FZD sensing platform so far. Therefore, the development of a photo-assisted electrochemical sensor using a spinel $CuCo_2O_4$-based electrode has novelty and is scientifically meaningful. The synergistic effects, optoelectronic properties, high electron mobility, and efficient light absorption of $CuCo_2O_4$ enhanced the responsivity and sensitivity in this configuration remarkably, suggesting engaging potential in ultrasensitive photo-electrochemical sensing devices.

Inspired by the characteristic properties and potential application of $CuCo_2O_4$, we proposed a strategy for the construction of a novel photoelectrochemical sensor for the detection of FZD antibiotic residues in food samples based on $CuCo_2O_4$ nanorods synthesized by a microwave-assisted hydrothermal method. In particular, in this work, the effect of green light illumination on the electrochemical behaviors and sensing performance was also examined in detail through electrochemical impedance spectroscopy (EIS), cyclic voltammetry (CV), differential pulse voltammetry (DPV), and chronoamperometry (CA) measurements, respectively. The possible photo-assisted electrochemical mechanisms were presented to clarify the changes in kinetic parameters during green light illumination. The repeatability, selectivity, stability, and actual applicability of the proposed photoelectrochemical sensing platform with green laser light irradiation were also examined carefully.

2. Experimental section

2.1. Chemicals

All the chemicals were utilized as received without any further purification. $Co(NO_3)_2 \cdot 6H_2O$ (98.5%), $CuCl_2 \cdot 2H_2O$ (99%), $(NH_2)_2CO$ (99%), $K_3[Fe(CN)_6]$ (99.5%), and $K_4[Fe(CN)_6]$ (99.5%)

were provided by Xilong Scientific Co, Ltd, China. Furazolidone (FZD, 98.5%) was purchased from Sigma-Aldrich. KCl (99.5%), KH_2PO_4 (99.5%), NaCl (99.5%), and $Na_2HPO_4 \cdot 12H_2O$ (99%) were manufactured by Guangdong, Guanghua Chemical Factory Co. Ltd, China, and Merck KgaA for preparation of 0.1 M phosphate-buffered saline (PBS) (pH 7.3). For controlling pH of PBS solution, H_3PO_4 (85%) and NaOH (96%) from Duc Giang Detergent Chemical. JSC, Vietnam were added. Besides, the double-distilled water was utilized in solutions throughout the entire experiment was purified through a Bibby (stuart) A4000D machine (United Kingdom).

2.2. Synthesis of $CuCo_2O_4$ and fabrication of $CuCo_2O_4$-modified SPE electrode

$CuCo_2O_4$ nanorods (CCO) sample was fabricated by a microwave-assisted hydrothermal method. Initially, $Co(NO_3)_2 \cdot 6H_2O$ (10 mmol) and $CuCl_2 \cdot 2H_2O$ (5 mmol) were dissolved in 250 ml of double-distilled water by magnetic stirrer for 15 minutes at room temperature. The mixture is then slowly added 50 ml $(NH_2)_2CO$ (60 mmol) and constantly agitated for 30 minutes. The resultant solution was then relocated into a 500 ml high-pressure reaction vessel in a microwave reactor system and heated at 160 °C for 20 minutes with microwave power of 500 W to begin the microwave-assisted hydrothermal process. The reaction vessel was cooled down naturally to room temperature when the reaction was completed. The dark blue precipitates were treated numerous times in double-distilled water and ethanol to remove residual by-products, and dried at 80 °C for 12 hours. The $CuCo_2O_4$ powder sample eventually was obtained after calcined in air at 400 °C for 2 hours.

Screen-printed electrode (SPE) was provided by Metrohm Vietnam Co, Ltd (Vietnam). Initially, the bare SPEs were washed numerous times with ethanol, double-distilled water and then dried naturally before modification. The modified electrodes were fabricated by a simple dropping method. A certain amount of $CuCo_2O_4$ powder was dispersed in double-distilled water and sonicated for 1 hour to get homogeneous suspension (1 mg ml^{-1}). Then, 8 μL of the homogeneous suspension was dropped onto the surface of the working electrode and dried for at 40 °C for 120 minutes. Finally, the $CuCo_2O_4$-based modified SPE electrode (CCO/SPE) was carefully stored in the dry air before using for the further electrochemical experiments.

2.3. Instruments and measurements

The $CuCo_2O_4$ nanomaterial was synthesized by the UWave-2000 Multifunctional microwave chemistry reaction workstation, SINEO, China. The crystalline structure of the CCO samples analyzed using by X-ray diffraction spectra obtained from a Bruker D5005 X-ray Diffractometer with Cu Kα radiation ($\lambda = 0.154056$ nm). The UV-vis absorbance spectra were recorded using an HP 8453 spectrophotometer over a wavelength range of 200 to 900 nm. The Raman measurements were conducted using a MacroRAM™ from Horiba Scientific with a 785 nm excitation laser source. The morphology of the $CuCo_2O_4$ material was examined by a scanning electron microscope (SEM) system. The pH measurements were conducted utilizing

a Benchtop pH Meter (Laqua pH 1200). All the electrochemical measurements were carried out at room temperature using a Palmsens4 electrochemical workstation (Palmsens, The Netherlands). The PBS solution served as the electrolyte, along with the SPE modified with $CuCo_2O_4$ served as the working electrode. For all experiments that required laser light support, a laser source with a wavelength of 500 nm (green) with a power density of 50 mW nm^{-2} was used to examine the effect of photo-assisted on the electrochemical behaviors and sensing performance for FZD detection.

The electrochemical characteristics of pure SPE and $CuCo_2O_4$-modified SPE electrode were investigated by measuring electrochemical impedance spectroscopy (EIS), cyclic voltammetry (CV), differential pulse voltammetry (DPV), and chronoamperometry (CA) at different setup conditions. Firstly, the electrochemical measurements, including the EIS and CV measurements, were executed in a 0.1 M KCl solution containing 5 mM $K_3[Fe(CN)_6]/K_4[Fe(CN)_6)]$ as redox probes. Namely, EIS experiments were carried out in the frequency range of 0.01 Hz to 50 kHz with an applied ac potential of – 0.25 V. Besides, CV measurements were measured by applying a potential from – 0.3 to 0.6 V at various scan rate from 10 to 60 mV s^{-1}. Secondly, the electrochemical performance of FZD on the bare SPE and modified SPE electrodes in without and with photo-assisted was investigated *via* CV, CA, and DPV techniques in a 0.1 M PBS solution. The CV measurements were conducted within a potential range of −1.0 to 0 V at various scan rates between 20 and 80 mV s^{-1}. CA measurements were conducted at the potential of −0.4 V in the presence of 100 μM FZD. The DPV measurements were done under the specified conditions such as scan rate of 0.006 V s^{-1}, $T_{equilibrium}$ = 120 s, E_{pluse} = 0.075 V, and T_{pulse} = 0.2 s, respectively. The limit of detection (LOD), the limit of quantification (LOQ), and the sensitivity of the proposed electrochemical sensor were determined by using the following equations:

$$LOD = 3.3\sigma/S;$$

$$LOQ = 10\sigma/S;$$

$$Sensitivity = S/A$$

where S is the slope of the calibration curve, σ is the standard deviation for 20 replicates of blank sample, and A is the electrochemical active surface area (EASA) of electrodes.

3. Results and discussion

3.1. Structural and morphological analysis of $CuCo_2O_4$

The crystalline structure and phase formation of the $CuCo_2O_4$ material by the microwave-assisted hydrothermal method were scrutinized by XRD analysis and are shown in Fig. 1a. The observed diffraction peaks in both samples at 18.92°, 31.11°, 36.75°, 38.55°, 44.62°, 48.87°, 55.34°, 59.27°, and 65.17° are assigned to the (111), (220), (311), (222), (400), (331), (422), (511) and (440) crystal planes, respectively. These diffraction patterns are in accordance with JCPDS card No. 01-1155 for the crystalline cubic spinel phase in the cubic $Fd\bar{3}m$ space group of $CuCo_2O_4$.[21,28] Also, no other phase peaks are observed, indicating the phase purity of $CuCo_2O_4$ sample. The average crystallite size of $CuCo_2O_4$ was determined at about 11.71 nm by the Scherrer's formula[13,29] through the (311) plane: $D = 0.9\lambda/\beta \cos \theta$, where λ represents the X-rays wavelength (λ = 0.154056 nm), β denotes the full width at half maximum (FWHM) intensity measured in radians, θ signifies the Bragg diffraction angle of the plane, and D indicates the crystallite size (nm). Besides, the lattice parameter for cubical structure can be determined by the following formula: $d_{hlk} = \frac{a}{\sqrt{h^2 + k^2 + l^2}}$, where (hkl) denotes the lattice plane index, d-spacing (interplanar spacing), a signifies lattice constant, and h, k and l are all integers. The lattice parameter value was calculated to be 8.103 Å through the strongest peak (311), which corresponded to the pure cubic spinel phase of $CuCo_2O_4$ with a lattice parameter value of a = 8.128 Å.[30] The lattice parameter value is smaller than along the (311) in the prepared $CuCo_2O_4$, attributable to the lattice strain caused by the elevated surface area to volume ratio. Jiang *et al.*[31] pointed out that the decline in size is accountable for the lattice contraction.

Raman spectroscopy analysis was utilized to further identify structural features of the $CuCo_2O_4$, as depicted in Fig. 1b. Five distinguishable Raman peaks are located at approximately 204.33 cm^{-1}, 491.03 cm^{-1}, 527.29 cm^{-1}, 625.74 cm^{-1}, and 692.67 cm^{-1}, corresponding to the characteristic bands ($3F_{2g}$ + E_g + A_{1g}) of $CuCo_2O_4$.[24,32] This obtained result further confirms the existence of the $CuCo_2O_4$ nanocrystals. Besides, the bonding characteristics of the $CuCo_2O_4$ sample were studied by FTIR spectroscopy at room temperature in the range 400–2000 cm^{-1} and shown in Fig. 1c. Two distinct bands were observed at ranging from 400 to 700 cm^{-1}, which are suitable with earlier reported literature. The bands at 547.29 cm^{-1} and 653.52 cm^{-1} are related with the stretching vibrations of Co^{3+}–O^{2-} and Cu^{2+}–O^{2-}, respectively.[33,34] In general, the presence of characteristic bands of $CuCo_2O_4$ in both FTIR and Raman results was recorded, demonstrating further that the $CuCo_2O_4$ sample was synthesized successfully with high purity, which is consistent with the observed XRD results.

The morphology of $CuCo_2O_4$ was investigated using scanning electron microscopy (SEM). The SEM micrographs in Fig. 1d of the $CuCo_2O_4$ powder displayed highly porous morphology with the particle aggregation. These $CuCo_2O_4$ nanocrystals are homogeneous in 20–25 nm-sized, oriented together to form one-dimensional porous nanorods with an average width of 80 nm and a length of 450 nm. It is thought that the high aspect ratio of the $CuCo_2O_4$ nanorods is believed to have a favorable effect on the conductivity and electrochemical performance.[18] On the other hand, with the unique feature of porous nanorods can provide high surface area and a great number of active sites for the redox reaction. Moreover, the porous structure allows easy penetration of the electrolyte, which can contribute to an enhancing in the catalytic activity.

The schematic illustration for the formation of $CuCo_2O_4$ nanorods through a microwave-assisted hydrothermal process is shown in Fig. 2a. During the synthesis procedure, in aqueous
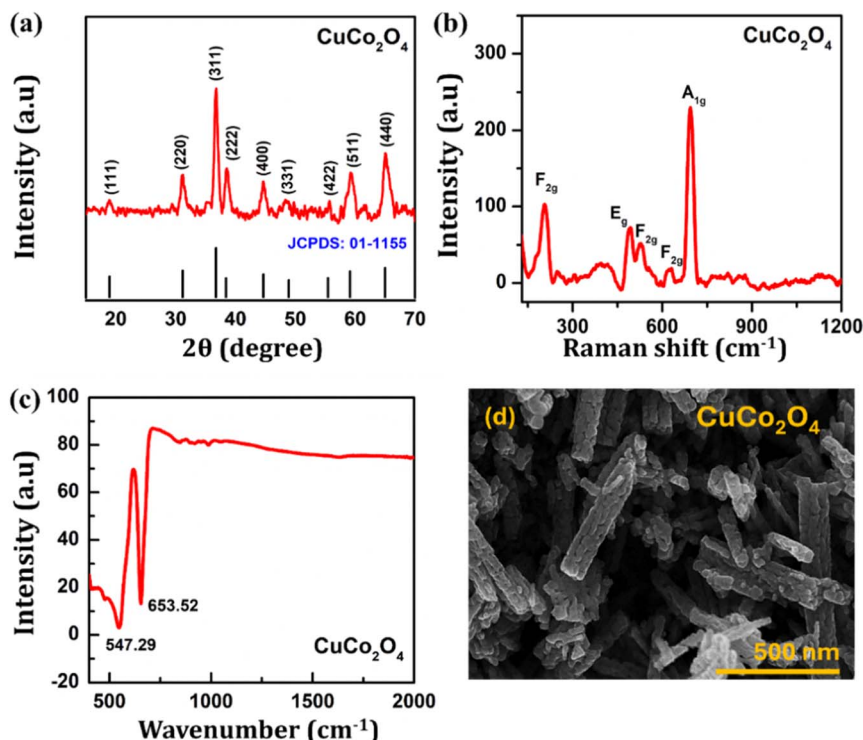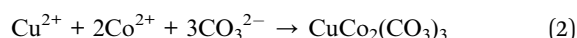
Fig. 1 (a) XRD pattern, (b) Raman spectrum, (c) FTIR spectra, and (d) SEM micrographs of CuCo$_2$O$_4$ nanorods.

solution, Cu^{2+} and Co^{2+} ions are generated from their respective salts. When the reaction mixture is heated, CO(NH$_2$)$_2$ liberates amoni (NH$_4^+$) ions and carbonate (CO$_3^{2-}$) anions (eqn (1)). From here, carbonate ions react with the metal precursors (Cu–Co) to form the corresponding carbonate salts (eqn (2)). After calcination at 400 °C for 2 hours, excess CO$_2$ is released and leads to the formation of CuCo$_2$O$_4$ (eqn (3)). The reaction succession during the synthesis of CuCo$_2$O$_4$ was proposed in the following equations:[35,36]

$$CO(NH_2)_2 + 2H_2O \rightarrow 2NH_4^+ + CO_3^{2-} \qquad (1)$$

$$Cu^{2+} + 2Co^{2+} + 3CO_3^{2-} \rightarrow CuCo_2(CO_3)_3 \qquad (2)$$

$$CuCo_2(CO_3) + \frac{1}{2}O_2 \rightarrow CuCo_2O_4 + 3CO_2 \qquad (3)$$

Herein, CO(NH$_2$)$_2$ is chosen as a forced-hydrolysis agent in this work as it acts as an effective oxidant and plays a role in stabilizing the nanostructure and also in the oriented growth of the nanorods.[37] CO(NH$_2$)$_2$ creates porosity in the nanostructure due to the ammonium ions are released as ammonia and water vapor. In addition, benefiting from the microwave heating process, the CuCo$_2$O$_4$ nanorods were fabricated a short time with uniform and controlled morphology due to the absence of thermal gradient effects (Fig. 2b).

The optical properties and optical band gap (E_g) of the CuCo$_2$O$_4$ nanorods were examined by UV-visible spectral analysis at room temperature, as displayed in Fig. 2c. The synthesized CCO sample displayed a high absorption band in the spectral range of 200 to 900 nm. Namely, three absorption peaks were observed: one absorption peak in ultraviolet at a wavelength of 254 nm and two absorption peaks observed in the visible light region at 450 nm and 760 nm.[38–40] The absorbance band at 200–300 nm was reported to be the existence of the cuprous oxide phase.[41] Meanwhile, two various absorbance bands at 760 nm and 450 nm were associated with the O^{2-} → Co^{3+} charge transfer (with the Co^{3+} level located below the conduction band) and the O^{2-} → Co^{2+} charge transfer process (valence to conduction band excitation), which shows the double oxidation state of cobalt elements.[17] In addition, the direct optical band gap for CuCo$_2$O$_4$ nanorods was calculated applying the Tauc's equation:[14] $\alpha h\nu = C(h\nu - E_g)^2$, where α is the absorption coefficient, $h\nu$ is the photon energy (eV), and C is proportionality constant. Fig. 2d exhibits the curve of $(\alpha h\nu)^2$ *versus* the photon energy ($h\nu$). From here, the E_g was calculated by extrapolating the linear part of the curve to zero. Two direct E_g values of CuCo$_2$O$_4$ nanorods were found to be 1.69 and 2.41 eV, which were well matched with previously reported results for CuCo$_2$O$_4$ nanomaterial and CuCo$_2$O$_4$ thin films formed at various temperatures.[40,42,43] It suggests that the as-synthesized CCO sample, characterized by low optical band gap values, can be readily stimulated and effectively absorb visible light. This makes CuCo$_2$O$_4$ nanorods a promising electrode candidate for a photoelectrochemical sensor that uses visible light-assisted platform to achieve high efficiency and outstanding sensitivity. Additionally, the maximum wavelength of radiation that the CuCo$_2$O$_4$ nanorods can absorb and promote electrons from the valence band to the conduction band was also calculated *via* the formula: $\lambda = hc/E_g$. The
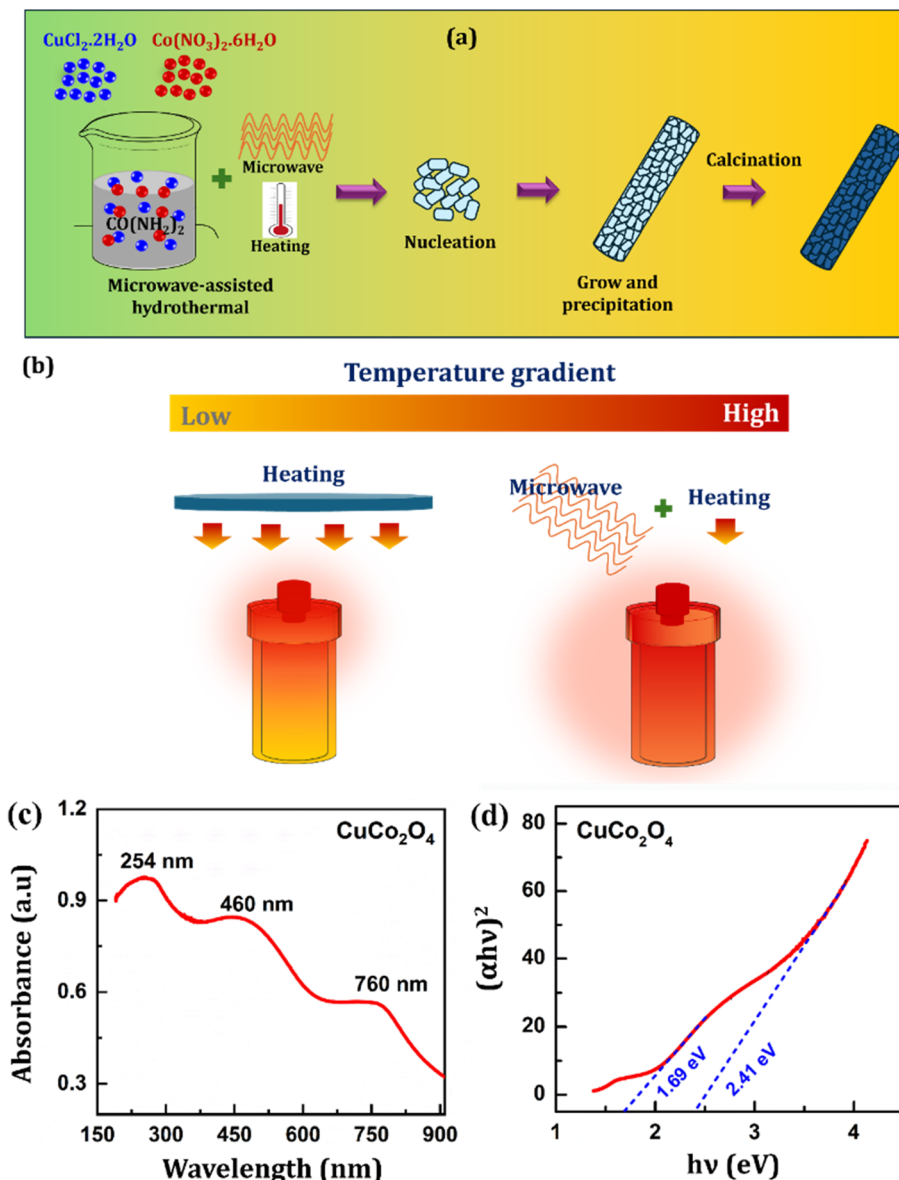
Fig. 2 (a) Schematic representation for the formation mechanism $CuCo_2O_4$ nanorods, and (b) comparison of conductive and microwave heating process, (c) UV-Vis absorption spectra, and (d) the Tauc plot and optical band gap values of $CuCo_2O_4$ nanorods.

wavelengths were found to be approximately 734 nm and 515 nm for the optical band gap to be 1.61 eV and 2.41 eV, respectively. On the other hand, the largest absorption band in the visible region of $CuCo_2O_4$ is in the wavelength range from 380 nm to 600 nm. Therefore, we selected a 500 nm wavelength of the green laser pointer pen, which belongs to the largest absorption band in the visible region, and ensure the condition of excitation light's energy is higher than the band gap energy, as the illumination source for electrochemical experiments that use a photo-assisted platform.

3.2. Electrochemical characteristics of CCO-modified SPE electrode

To study the electrochemical properties of unmodified and modified SPE electrodes, electrochemical impedance spectroscopy (EIS) and cyclic voltammetry (CV) methods were performed in a 0.1 M KCl solution containing 5.0 mM $K_3[Fe(CN)_6]$ and $K_4[Fe(CN)_6]$. Firstly, EIS measurements were carried out to find out the charge transfer resistance (R_{ct}) value, intended to assess the electronic conductivity at the electrode–electrolyte interface on the electrodes. Fig. 3a displays the Nyquist plots obtained over the frequency range from 0.01 Hz to 50 kHz and Randles equivalent circuit model (as shown in the inset). The R_{ct} value is determined in the high frequency range through the semicircle diameter. In the Nyquist plot, the R_{ct} value is determined in the high frequency range through the semicircle diameter. Mixed kinetic-control and diffusion-control processes are represented by a linear portion in the lower frequency range.[44] Herein, Randle's equivalent circuit was used to fit Nyquist plots of pure SPE and $CuCo_2O_4$-based
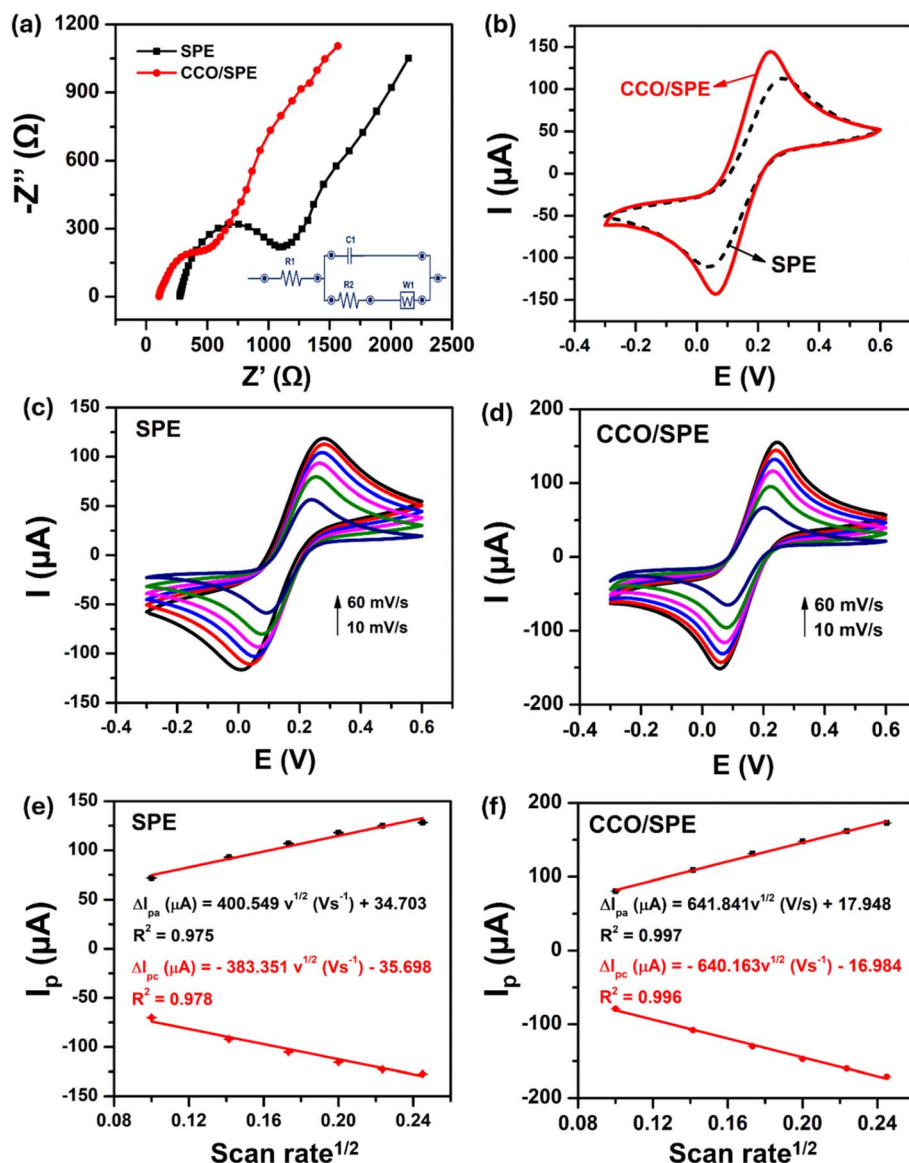
Fig. 3 Nyquist plot (a) and CV profiles (b) of pure SPE, and CCO-modified SPE electrode. (c–f) CV curves recorded on SPE and CCO/SPE in 0.1 M KCl containing 5 mM $K_3[Fe(CN)_6]$ and $K_4[Fe(CN)_6]$ at different scan rates, corresponding to the linear graphs of peak current response (I_{pa}, I_{pc}) *versus* $v^{1/2}$ with error bars.

modified SPE electrodes (Fig. S1†). In which, R_2 is R_{ct}, which refers to the electron transfer resistance across the electrode–electrolyte interface. According to that, the R_{ct} values could be estimated as 680.7 Ω for bare SPE and 332.1 Ω for CCO/SPE. It can be clearly observed that the modified electrode based on $CuCo_2O_4$ could decrease charge transfer resistance, leading to the higher conductivity. The R_{ct} value of the smaller modified electrode could be attributed to the higher crystallinity of $CuCo_2O_4$ nanorods, which made the charge transfer easier.

In addition, to further understand the role of $CuCo_2O_4$ nanorods in promoting electro-reduction peak current as well as electrochemical active surface area (EASA) and decreasing peak-to-peak potential ($\Delta E_p = E_{pa} - E_{pc}$), the CV investigations at different scan rates with a voltage window of – 0.3 to 0.6 V (Fig. 3b–f). Herein, Fig. 3b displays the CV curves of pure SPE

and CCO/SPE at a scan rate of 50 mV s^{-1}. The obtained CV curves showed a pair of redox peaks, corresponding to the reversible redox process of Fe^{2+}/Fe^{3+}.[14] Notably, the results exhibited that the redox peak current responses of CCO-modified SPE electrode were 162.5 and 160.7 µA, which were 29.7 and 31.08% higher than that of the bare SPE (125.3 and 122.6 µA), respectively. Moreover, the peak-to-peak separation (ΔE_p) between the reduction and oxidation potential for CCO/SPE was determined to be 179 mV, which is significantly lower than the pure SPE (239 mV). Meanwhile, a limit in the charge transfer kinetics is indicated by the deviation of the ΔE_p value from the theoretical value of 0 mV.[12] This means that the modification of working electrode surface by $CuCo_2O_4$ nanorods brought many beneficial refinements in charge transfer and conductivity compared with bare SPE.
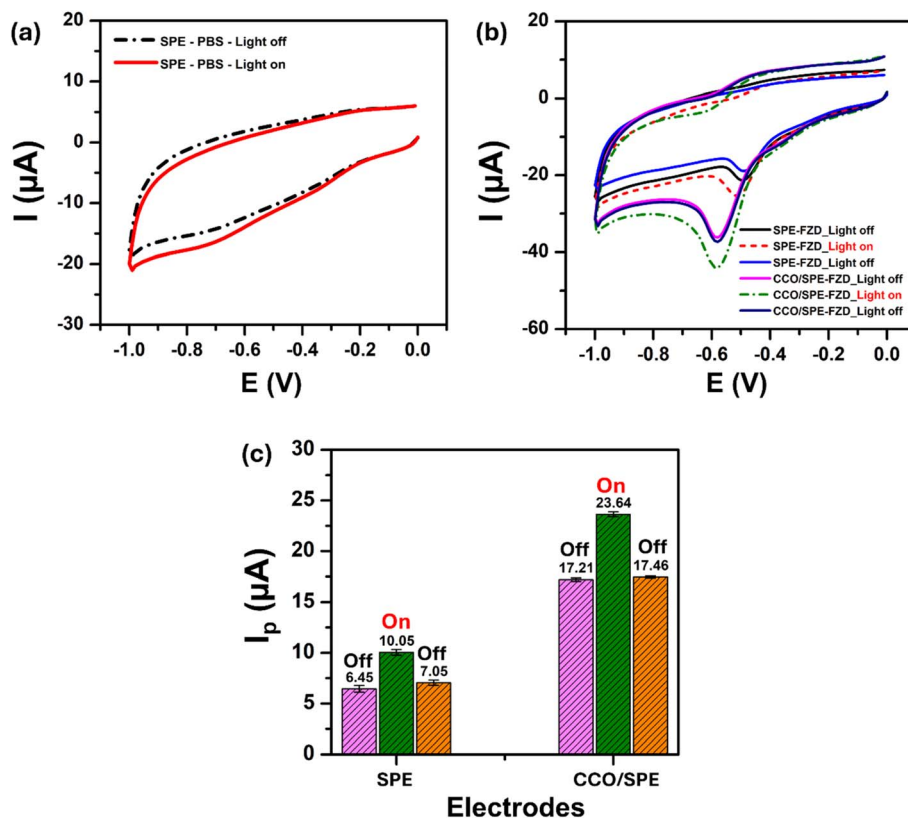
Fig. 4 CV voltammograms of SPE in 0.1 M PBS (pH 7.3) under both light-absent and light-present conditions; (b) CV curves exhibiting "off–on–off" behavior were obtained from on bare SPE and CCO/SPE in 0.1 M PBS (pH 7.3) with 200 µM FZD; (c) the corresponding bar chart diagram of electro-reduction peak currents with error bars. Scan rate: 50 mV s^{-1}.

Additionally, when CV measurements were carried out at different scan rates in the range from 10 to 60 mV s^{-1} on the unmodified and modified SPE electrodes, the changes in current intensity and the reversible oxidation and reduction peak potential were observed and exhibited in Fig. 3c and d. In this case, it can be seen that the anode (ΔI_{pa}) and cathode (ΔI_{pc}) peak current value linearly increased with an increase of the square root of the scan rate ($\nu^{1/2}$), corresponding to the regression equations (Fig. 3e and f):

$$\Delta I_{pa} \ (\mu A) = 400.549\nu^{1/2} \ (V \ s^{-1}) + 34.703 \ (R^2 = 0.975),$$

$$\Delta I_{pc} \ (\mu A) = -383.351\nu^{1/2} \ (V \ s^{-1}) - 35.698 \ (R^2 = 0.978)$$
$$\text{for bare SPE, and}$$

$$\Delta I_{pa} \ (\mu A) = 641.841\nu^{1/2} \ (V \ s^{-1}) + 17.948 \ (R^2 = 0.997),$$

$$\Delta I_{pc} \ (\mu A) = -640.163\nu^{1/2} \ (V \ s^{-1}) - 16.984 \ (R^2 = 0.996)$$
$$\text{for CCO/SPE.}$$

This suggests that the oxidation and reduction reaction onto the electrode surfaces of SPE and CCO/SPE was a diffusion-controlled process.[7,45] According to that, the electrochemical active surface area (EASA) value, which reflects the total electrochemical active area, was calculated *via* the Randles–Sevcik equation: $\Delta I_p = 2.69 \times 10^5 n^{3/2} D^{1/2} A C \nu^{1/2}$, where A refers to the

electrochemical active surface area (EASA), D is the diffusion coefficient of K$_3$[Fe(CN)$_6$] and K$_4$[Fe(CN)$_6$] ($D = 6.5 \times 10^{-6}$ cm^2 s^{-1}), C is the concentration of K$_3$[Fe(CN)$_6$] and K$_4$[Fe(CN)$_6$] solution, n is the number of electron transferred in the redox reaction, ν is the scan rate (mV s^{-1}), and ΔI_p (µA) is the oxidation/reduction peak current. According to that, the EASA values of CCO/SPE were determined to be 0.187 cm^2, which was ~67% greater than that of the pure SPE (0.112 cm^2). On the other hand, the previous reports pointed out that the higher the EASA, the enhanced accessibility of analytes to the electrochemically active sites.[7,46] In addition, the EASA value for the CCO/SPE may be associated with its high active site density. Indeed, it has been explored that in cobalt oxide-based spinel structures, the surface Co^{3+} ions at octahedral sites are the active sites.[47] To sum up, with the achieved outcomes of CCO-modified SPE electrode such as higher the response peak current, lower electron transfer resistance (R_{ct}), smaller separation potential (ΔE_p), and larger EASA values than bare SPE, it implies that the CCO/SPE might provide interesting results for the electrochemical determination of FZD.

3.3. Electrochemical characterizations and optimization of experimental parameters

3.3.1 Electrochemical behaviors of FZD. To examine the electrochemical behaviors of FZD when with and without light-assisted on the CuCo$_2$O$_4$ nanorods-based electrochemical

sensing platform, CV measurements were conducted in a 0.1 M PBS buffer solution in the presence and absence of 200 μM FZD (Fig. 4a and b) under with and without light irradiation conditions. In Fig. 4a, in the absence of FZD, no redox peaks were observed within the potential range of 0–1.0 V in the PBS buffer solution on the bare SPE. However, the presence of green light resulted in a higher increase in background current than the without light condition. This implies that green light has a positive effect on electron transfer kinetics. Indeed, visible light can activate the surface centers of nanoporous carbons that were printed on the bare SPE working electrode, generating charge carriers (through radical formation). This makes chemical reactions more efficient.[48] Besides, the green light-assisted FZD electro-reduction was further examined by the CV measurements on both pure SPE and CCO/SPE in 0.1 M PBS solution containing 200 μM FZD at a scan rate of 50 mV s^{-1} in the with and without green light (Fig. 4b and c). For the bare SPE, the sharp reduction peaks were recorded at the potential of −0.49 V; meanwhile, this peak can be observed at a lower negative potential of −0.58 V for CCO/SPE. Similar electrochemical behaviors of FZD have also been reported in some previous studies.[6,19,49] Besides, the difference in electron transportability between bare SPE and CCO/SPE (as results found in Nyquist plots) was believed to lead to the shift reduction FZD of CCO/SPE compared with bare SPE. Furthermore, in the absence of light, the FZD reduction peak current of CCO/SPE (6.45 μA) was 166.82% higher than pure SPE (17.21 μA) and there is

a 0.093 V change toward a more negative potential, from −0.489 V of pure SPE to −0.582 V for CCO/SPE. This exhibited that the modification of working electrode surface of SPE with CuCo$_2$O$_4$ nanorods was significantly enhanced FZD reduction peak current and decreased peak current.

More interestingly, with the green light source turned on, the FZD peak current response increases and the reduction peak potential shifts to a more negative value. Namely, the peak current of FZD observed at unmodified electrode (10.05 μA) and CCO-modified SPE electrode (23.64 μA) were approximately 3.60 and 6.43 μA greater than that of the absence of green light. It is clear that with photo-assisted, CCO/SPE with larger signal increment of the FZD peak current showed strong photocatalytic activity toward the reduction of FZD. On the other hand, the FZD cathode peak current and peak potential return to their initial dark values when the light is turned off. This indicates that the CCO-modified SPE electrode responds significantly to green light, confirming the clear effect of green light on an enhanced FZD electrochemical reduction process.

3.3.2 Study on the effect of scan rate. In order to gain insight into the effect of green light on the electrochemical reduction kinetics, the influence of scan rate on reduction peak current of FZD was studied by CV measurements. Fig. 5 and 6 display the CV curves of the CCO/SPE in 0.1 M PBS solution containing 200 μM FZD at various scan rates from 20 to 80 mV s^{-1} in the absence and presence of green light, respectively. As can be seen, Fig. 5a and 6a show the electro-reduction peak
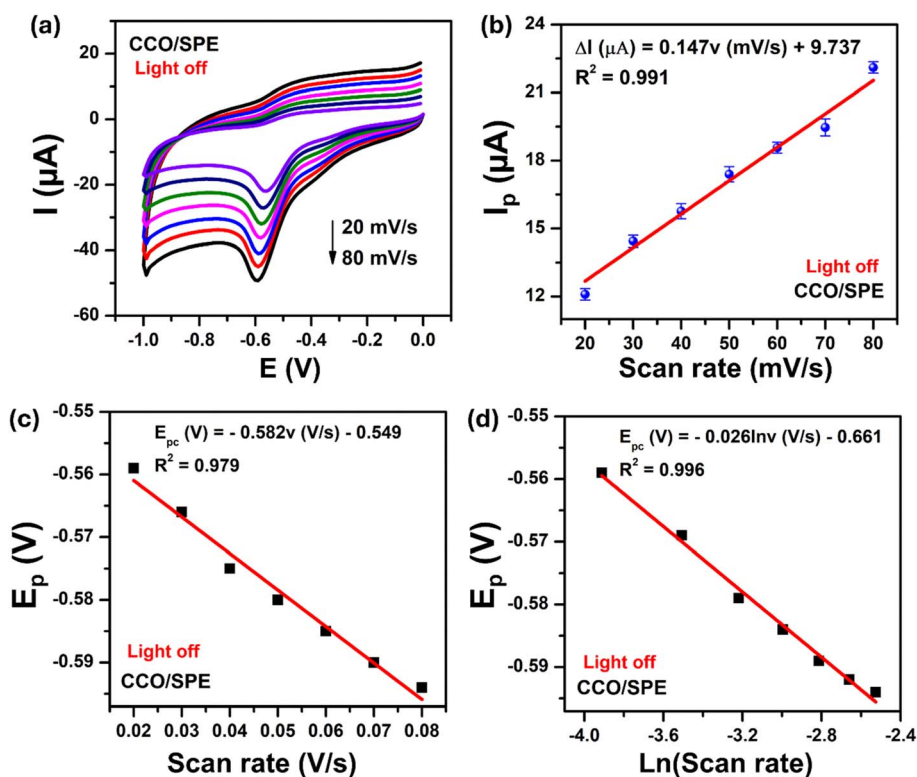

Fig. 5 (a) CV curves of CCO/SPE were recorded in 0.1 M PBS (pH 7.3) containing 200 μM FZD, (b) linear plot for scan rate *vs.* FZD electro-reduction peak current, (c) linear graph for scan rate *versus* FZD electro-reduction peak potential (E_{pc}), and (d) the plot of E_{pc} with the natural logarithm of scan rate [ln(ν)].
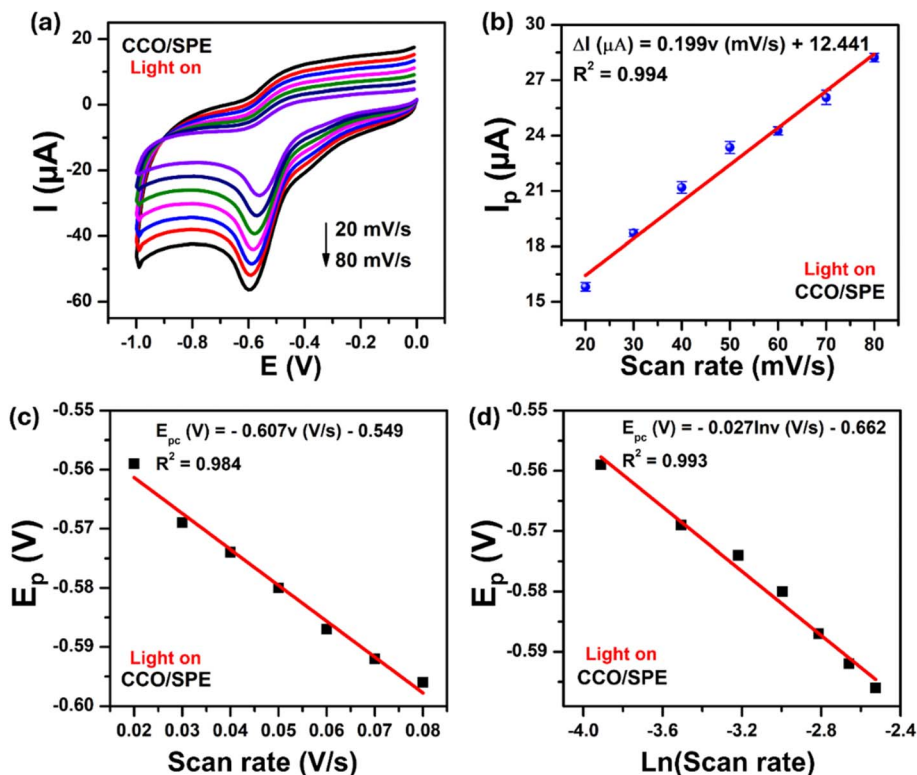
Fig. 6 (a) CV voltammograms of CCO/SPE in 0.1 M PBS (pH 7.3) containing 200 μM FZD at various scan rates from 20 to 80 mV s^{-1}, (b) a linear relationship between electro-reduction peak current and scan rate, (c) linear graph for scan rate *versus* E_{pc}, and (d) the plot of E_{pc} with the natural logarithm of scan rate [ln(ν)] in the presence of light-assisted.

current of FZD significantly increased upon increasing the scan rate, indicating that the electrochemical reduction of FZD is the surface adsorption–controlled process.[6,7] Additionally, when with and without green light irradiation, an excellent linear dependence between the electro-reduction peak currents and the scan rates was observed in Fig. 5b and 6b, corresponding to the linear regression equations to be:

$$I_p \, (\mu A) = 0.147\nu \, (\text{mV s}^{-1}) + 9.737 \, (R^2 = 0.994)$$
(without green light),

$$I_p \, (\mu A) = 0.199\nu \, (\text{mV s}^{-1}) + 12.441 \, (R^2 = 0.994)$$
(with green light)

Besides, the shifts of the peak potential of FZD were recorded following the difference scan rates. Indeed, the cathode peak potentials (E_{pc}) of FZD shifted toward the negative direction in a linear relationship with the natural logarithm of scan rate [ln(ν)], corresponding to a regression equation as $E_{pc} = -0.026$ ln(ν) $- 0.061$ ($R^2 = 0.996$) in the absence of green light irradiation, and $E_{pc} = -0.027$ ln(ν) $- 0.062$ ($R^2 = 0.993$) in the presence of green light irradiation. On the other hand, Laviron's equation for an irreversible electrode process, the relationship between E_{pc} and scan rate was to be:[6,7,50]

$$E_{pc} = E^0 + (RT/\alpha nF)\ln(RTk_s/\alpha nF) - (RT/\alpha nF)\ln(\nu)$$

where α is the electron transfer coefficient, $T = 298$ K, n is the number of electrons transferred, R denotes the gas constant ($R = 8.314$ J mol^{-1} K^{-1}), k_s is the electron transfer rate constant, F is the Faraday constant ($F = 96\,485.33$ C mol^{-1}), and the formal redox potential (E^0) value can be obtained from the intercept of E_{pc} *vs.* ν plot (Fig. 5c and 6c). With the slope of a straight-line plot yielding equal with $RT/\alpha nF$, thus, k_s values of CCO/SPE in the presence and absence of green light were calculated at 0.518 s^{-1} and 0.564 s^{-1}, respectively. Simultaneously, the number of electrons transferred (n) was estimated to 2, and the electron transfer coefficient values (α) of CCO/SPE were calculated to be approximately 0.494 and 0.475 for the absence and presence of green light cases, respectively. This achieved results well-matched with some previously proposed reports.[6,7,51] Hence, it can be inferred that the number of electrons involved in the electrochemical reduction of FZD is two electrons. In addition, from the slope value of I_p *vs.* scan rate, the adsorption capacity (Γ) of FZD was determined by using equation with A is the EASA value (cm^2):

$$I_p = n^2F^2A\Gamma\nu/4RT$$

According to that, the Γ values on CCO-modified SPE electrode in the presence and absence of green light were determined to be 2.09×10^{-7} and 2.83×10^{-7} mol cm^{-2}. The obtained k_s and Γ values of CCO/SPE with the assistance of

green light were 8.88 and 35.41% larger than those of in the no light condition, respectively. Besides, the values of α, n, and k_s exhibited no significant increases. Nevertheless, the adsorption capacity (Γ) of FZD on the CCO/SPE increased more than 35% relative to the initial value. This indicates that the green light irradiation significantly influenced the adsorbability and electron transfer kinetics of FZD on the CCO-based electrochemical sensing platform.

3.3.3 Chronoamperometry study. To further understanding of the influence of green light on electrocatalytic activity within CCO/SPE, chronoamperometry (CA) measurements were conducted by setting potential at -0.6 V in 20 seconds under with and without light conditions to determine the catalytic rate constant (k_{cat}). As illustrated in Fig. 7, in both two cases at 100 µM FZD concentration, the linear increase of reduction current response with the square root of time ($t^{1/2}$), corresponding with linear regression lines:

$$I_{cat}/I_L = 0.186t^{1/2} - 1.644 \ (R^2 = 0.989) \ \text{(in the absence of green light irradiation)}$$

$$I_{cat}/I_L = 0.296t^{1/2} - 2.084 \ (R^2 = 0.996) \ \text{(in the presence of green light irradiation)}$$

On the other hand, according to the Galus method through formula:[14,52] $I_{cat}/I_L = (\pi t)^{1/2}(k_{cat}C_0)^{1/2}$, where I_{cat} and I_L are the currents at the CCO/SPE in the presence and absence of FZD, t is practiced measurement time (s), and C_0 is the bulk concentration of FZD, respectively. Herein, based on the direct slope values seen in Fig. 7b, the k_{cat} was determined to be 0.110 M^{-1} s^{-1} and 0.279 M^{-1} s^{-1} without and with the assistance of green light, respectively. Clearly, under the assistance of green light, the k_{cat} values were enhanced significantly, approximately 153.64%, which shows that the presence of green light offered numerous beneficial enhancements in the electrocatalytic activity of the CuCo$_2$O$_4$-modified electrode.

3.3.4 Study on the effect of pH and accumulation time. Because the effect of the protonation has a significant impact on the overall electrochemical processes, the influence of the pH of

PBS buffer solution on the electrochemical responses was thoroughly examined on CCO/SPE for the FZD analyte in the presence of green light. DPV measurements recorded the changes to both the peak potential and peak current of FZD in a 0.1 M PBS solution with pH 3 to pH 11. As shown in Fig. S2a,† the reduction peak of FZD gradually enhanced as pH increased from 3.0 to 7.0; then there was a sharp reduction in electrochemical response for pH values between 7.0 and 11.0. The peak current reached a maximum at pH 7.0. Thus, pH 7.0 was selected as the optimal pH value for the following analytical experiments. Also, there was a significant negative shift in peak potential upon increasing the PBS solution pH, indicating that protons were engaged in the FZD reduction process. The relationship between pH values vs. E_{pc} is linear with the equation: E_{pc} (V) $= -0.029$pH $- 0.187$ ($R^2 = 0.998$) in Fig. S2b.† The slope value of 0.029 V per pH was the same as the Nernst equation of $dE_p/dpH = (2.303mRT)/(nF)$,[53,54] in which n and m stand for the number of electrons and protons intervening in the reduction process of FZD. As a result, the $m:n$ value was calculated at nearly 0.49. Besides, with the number of electrons calculated to be about two electrons in the scan rate section, which means that the number of protons in the reduction was determined at one proton. Thus, two electrons and one proton were involved in the electrochemical reduction process of FZD occurring at the electrode surface.[6,55] These results are well-fitted with some previously reported results for the electrochemical reaction of FZD.

The influence of the accumulation time played a crucial role in the electrochemical reaction. Hence, the effect of the accumulation time on the electrochemical response of CCO/SPE towards 200 µM FZD in 0.1 M PBS has been tested in the range from 10 to 210 s (Fig. S2c and d†). It can be seen that the reduction peak current increased steadily as the accumulation time grew from 10 to 130 s. However, from 130 s to 210 s, the peak current slightly enhanced. Namely, the accumulation time is increasing by 61.54% (from 130 s to 210 s); however, the peak current is only larger than 5.5% (18.23 µA to 19.17 µA). Thus, the optimized accumulation time of 130 s was selected for the next experiments.

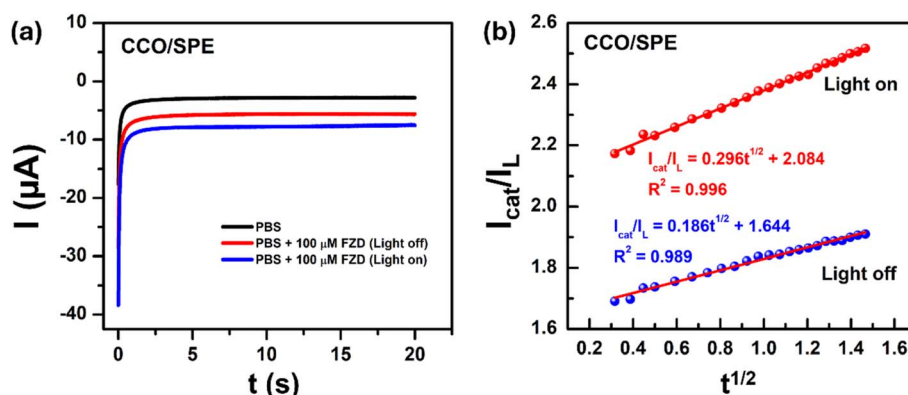**Fig. 7** (a) Chronoamperometric curves of the CCO/SPE in the absence and presence of 100 µM FZD in 0.1 M PBS solution under turn on and off light conditions; (b) the plot of I_{cat}/I_L vs. $t^{1/2}$ obtained from the chronoamperograms.
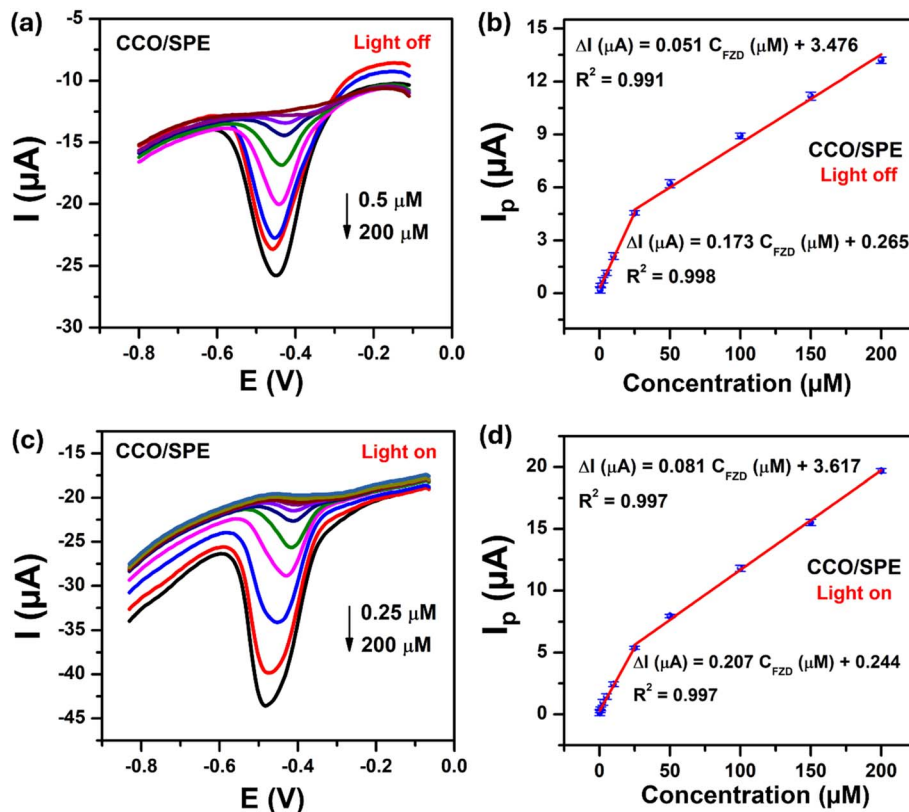
Fig. 8 (a and c) DPV curves recorded at the CCO-modified SPE in 0.1 M PBS (pH = 7.0) containing different concentrations of FZD without and with green light, respectively; (b and d) the plots of peak current as a function of FZD in the various concentration ranges.

3.4. Sensitive detection of furazolidone

Under optimized experimental conditions, the DPV technique was used to investigate the effect of green light on dynamic linear range, limit of detection (LOD), limit of quantification (LOQ), and electrochemical sensitivity toward the detection of FZD. Fig. 8a and c display DPV curves of CCO/SPE in 0.1 PBS (pH 7.0) containing various concentrations of FZD without and with the assistance of green light, respectively. As can be seen, the reduction peak current of FZD enhanced with the increasing of the FZD concentration analyte in both cases. Nevertheless, with the assistance of green light, CCO/SPE acquired a wider dynamic linear range in the concentration range of 0.25 to 200 μM, while CCO/SPE showed a linear range in the concentration range of 0.5 to 200 μM under turn-off green light source conditions. More intriguingly, the green light-assisted FZD electrochemical sensor's exceptional improvement in electron transfer kinetics and electrocatalytic activity resulted in superior analytical performance for FZD detection. Namely, Fig. 8b and d show the linear relationship between I_p and the FZD concentration with a linear equation:

Without green light irradiation

$$\Delta I \, (\mu A) = 0.051 C_{FZD} \, (\mu M) + 3.476 \, (R^2 = 0.991)$$
$$\text{for concentration FZD from 25–200 μM,}$$

$$\Delta I \, (\mu A) = 0.173 C_{FZD} \, (\mu M) + 0.265 \, (R^2 = 0.998)$$
$$\text{for concentration FZD from 0.5–25 μM}$$

With green light irradiation

$$\Delta I \, (\mu A) = 0.081 C_{FZD} \, (\mu M) + 3.617 \, (R^2 = 0.997)$$
$$\text{for concentration FZD from 25–200 μM,}$$

$$\Delta I \, (\mu A) = 0.207 C_{FZD} \, (\mu M) + 0.265 \, (R^2 = 0.998)$$
$$\text{for concentration FZD from 0.25–25 μM.}$$

With the observed slope values, the LOD and LOQ values were found at about 0.09 and 0.28 μM for CCO/SPE without green light irradiation, 0.03 and 0.09 μM for CCO/SPE with green light irradiation, respectively. The sensitivity of the CCO-based FZD sensing platform under green light irradiation was determined to be 1.11 μA μM^{-1} cm^{-2}, higher than of the turn-off light condition (0.93 μA μM^{-1} cm^{-2}).

3.5. Discussion on the enhancement mechanism of electrochemical characteristics & sensing performance in CCO-modified SPE

First and foremost, based on obtained outcomes towards $K_3[Fe(CN)_6]/K_4[Fe(CN)_6]$ detection such as lower electron transfer resistance (R_{ct}), smaller separation potential (ΔE_p), and higher EASA values than bare SPE, it implies that the CCO/SPE brought out an impressive enhancement in electrochemical properties. $CuCo_2O_4$ nanorods with the high crystallinity and
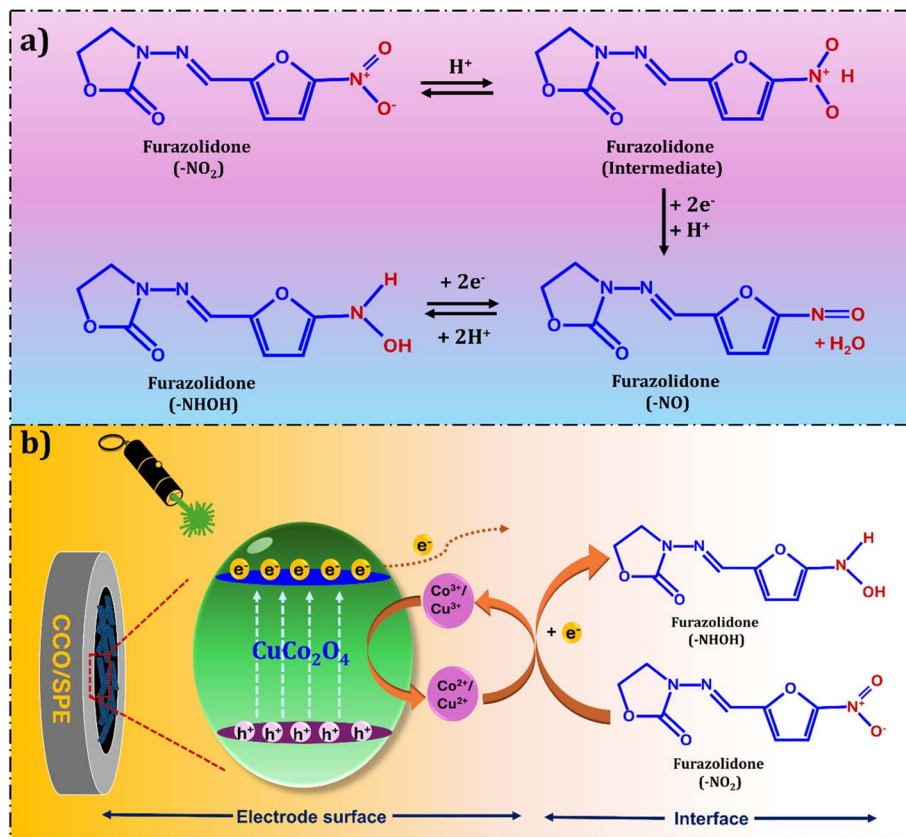
Fig. 9 (a) The electrochemical reduction mechanism of FZD, and (b) the enhancement mechanism of CuCo$_2$O$_4$-based photoelectrochemical sensor for detection of FZD under green light irradiation.

purity; besides, the existence of multiple valence states (Co^{2+}/Co^{3+} and Cu^{2+}/Cu^{3+}) structural lattice were beneficial to conductivity. This was confirmed through the remarkable decrease of R_{ct} and ΔE_p values compared with bare SPE. In addition, the porous nanorod-like structure of CuCo$_2$O$_4$ is thought to increase adsorption and facilitate the diffusion of electrolyte and target analyte. Secondly, as mentioned in the discussion of the study on the effect of scan rate and pH, the electrochemical reduction mechanism of FZD with SPE based on CuCo$_2$O$_4$ nanorods is proposed as shown in Fig. 9a by two processes: (i) the reduction process involves a nitro group (R–NO$_2$) of FZD forming a nitroso intermediate (R–N=O) group. (ii) The following process is the quick creation of hydroxylamine (R–NHOH). Herein, CuCo$_2$O$_4$ with the narrow bandgap values (1.6 eV and 2.41 eV) was excited easily by visible light to generate photo-induced electron–hole (e$^-$ and h$^+$) pairs. When in the presence of green light irradiation, the e$^-$ on the valence band (VB) will be excited to the conductive band (CB), leaving the h$^+$ on VB.[22] Then, both electrons and holes will migrate to the surface of the material. On the surface, electrons will donate to the electron acceptor, such as the –NO$_2$ group of FZD, which is reduced to its lower valence state –NHOH group (Fig. 9b). Furthermore, the possession of two band gap values with various energy levels existing in the CCO structure helps to prolong the electron–hole pair recombination time, leading to more e$^-$ and h$^+$ participating in the reduction reaction of FZD

occurring on the electrode surface. Thereby improving the electrocatalytic ability of CuCo$_2$O$_4$. On the other hand, the active sites are regenerated at the surface by electro-oxidation. The oxidation of Co^{2+} to Co^{3+} and Cu^{2+} to Cu^{3+} is followed by FZD reduction, and the rate of these reactions controls the sensing performance. The Co^{3+} and Cu^{3+} formed on the surface accept electrons from FZD and get reduced to Co^{2+} and Cu^{2+}.[20,56] The synergism of Cu and Co ions with different oxidation states was believed to provide more active sites and effectively improve the conductivity and catalytic activity. Thus remarkably enhancing the electrochemical FZD detection performance of the CuCo$_2$O$_4$ nanorods. Indeed, these explanations can be confirmed in the comparison of characteristic parameters of the photo-electrochemical sensors on CCO/SPE for detection of FZD in the absence and presence of green light illumination, as recapitulated in Table 1. For catalytic rate constant (k_{cat}) and adsorption capacity (Γ) values, it showed outstanding enhancement of about 153.6% and 35.5%, respectively; however, the transfer rate constant (k_s) value just exhibited a rather humble change for the better of 8.9% under green light irradiation. In addition, the impressive results were obtained for CCO/SPE in the presence of green light, such as 37.36% larger peak current response (I_p), wider linear range, a lower limit of detection and quantification, and 19% higher sensitivity compared with CCO/SPE without laser light irradiation, indicating that the laser light illumination has notably influenced kinetic parameters as well

Table 1 The characteristic parameters of the green light-assisted electrochemical sensor based on CuCo$_2$O$_4$-modified SPE electrode without and with the assistance of green light

| No.	Electrochemical kinetic parameters	Without green light	With green light	Variance (%)
1	Peak current response I_{pc} (µA)	17.21	23.64	37.36
2	Electron transfer rate constant k_s	0.518	0.564	8.88
3	Adsorption capacity Γ (mol cm^{-2})	2.09×10^{-7}	2.83×10^{-7}	35.41
4	The catalytic rate constant k_{cat} (M^{-1} s^{-1})	0.110	0.279	153.64
5	Linear range (µM)	0.5–200	0.25–200	—
6	Limit of detection LOD (µM)	0.09	0.03	200
7	Limit of quantification LOQ (µM)	0.28	0.09	190
8	Sensitivity (µA µM^{-1} cm^{-2})	0.93	1.11	19.35
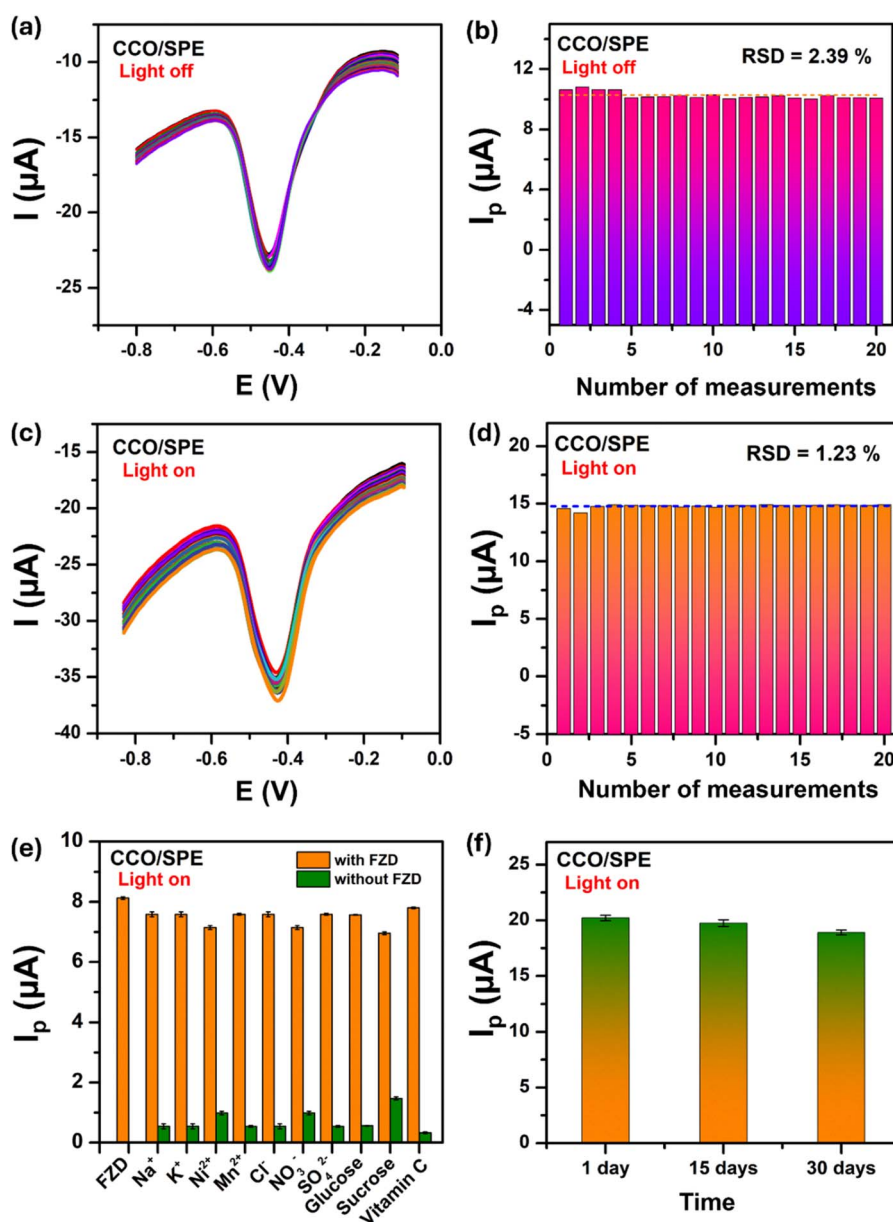
Fig. 10 The repeatability of CCO/SPE in 0.1 M PBS (pH 7.0) containing 100 µM FZD without (a and b) and with (c and d) of green light; (e) the anti-interfering capability in 0.1 M PBS containing 50 µM FZD and 1000 µM interfering substances in the assistance of green light; (f) the stability in 30 days with green light irradiation condition. The error bars denote the standard deviations from three independent experiments.

Table 2 Detection of FZD in milk and honey samples using the CCO/SPE ($n = 3$)

Electrode	Sample	Concentration (µM)		Recovery (%)	RSD (%)[n]
		Spiked	Found		
CCO/SPE (in the presence of green light)	Honey	10	9.556	95.56	2.97
		5	4.867	97.33	2.78
		2.5	2.387	95.46	4.01
	Milk	10	9.141	91.41	3.23
		5	4.809	96.17	1.09
		2.5	2.308	92.32	2.92

as electrochemical performance. Moreover, a comparison performance of our developed electrochemical sensing platform based on CuCo$_2$O$_4$ nanorods with previously reported electrochemical sensors using electrodes modified with spinel/oxide-based nanostructure for determination of FZD was summarized and listed in Table S1.† The results indicate the CCO-modified SPE electrode, with the assistance of green laser light, exhibits a high potential for ultrasensitive electrochemical detection of FZD in food samples.

3.6. Repeatability, anti-interference ability, stability, and real samples analysis

In order to look into the real-world uses of the suggested photoelectrochemical sensors, the crucial elements including stability, repeatability, and anti-interference ability were investigated. Foremost, the repeatability of the CCO-based photoelectrochemical sensor in the presence and absence of green light was scrutinized through 20 consecutive DPV measurements in 0.1 M PBS containing 100 µM FZD. As exhibited in Fig. 10a–d, the reduction peak current response of FZD without and with light irradiation displayed a negligible change, with the relative standard deviation (RSD) values found out to be 2.39% and 1.23%, respectively. Notably, incorporating green light into an CCO-based photoelectrochemical sensing platform surprisingly improves analytical performance while simultaneously increasing signal stability and repeatability for FZD determination.

The anti-interfering capability of the CCO/SPE under green-light irradiation is examined by the DPV technique in a PBS solution containing 50 µM FZD with the existence of some potential interfering substances found in milk and honey. Fig. 10e displays the change in the cathode peak current responses on CCO/SPE in the presence of several ions (Na$^+$, K$^+$, Ni^{2+}, Mn^{2+}, Cl$^-$, NO$_3^-$, and SO$_4^{2-}$), and some compounds (glucose, sucrose, and vitamin C), which are 20-fold more concentrated than FZD. The observed result showed that the 20-fold excess concentration of these interfering species has no explicit influence on the reduction peak current of FZD, suggesting that the proposed photoelectrochemical sensor has good anti-interfering capability for FZD determination.

The long-term stability of the green light-assisted FZD photoelectrochemical sensor was also examined carefully by measuring the peak current response of the CCO/SPE to 200 µM FZD over 15 and 30 days. As can be seen from Fig. 10f, the CCO/SPE maintained about 97.9% and 92.5% of its initial cathodic peak current after being stored at ambient temperature for two

weeks and four weeks, which suggests that the green light-assisted FZD photoelectrochemical sensor's capacity for long-term storage and operational stability.

To evaluate the application potential and analytical reliability of the CuCo$_2$O$_4$ nanorod-based photoelectrochemical sensing platform, milk and honey samples were used to analyze the content of FZD. The recovery assays of FZD were performed using the DPV technique through the standard addition method under green light, and the achieved results are summarized in Table 2. The CCO-based photoelectrochemical sensor showed recoveries ranging from 91.41% to 97.33%, with RSD values less than 5.0% ($n = 3$), which was acceptable for actual applications. These obtained results exhibited the good application potential of the proposed green light-assisted photoelectrochemical sensor in actual determination and monitoring of trace FZD residue in milk and honey samples.

4. Conclusions

This work reported a simple synthetic method for a CuCo$_2$O$_4$ nanorods aiming to modify the working electrode surface of commercial SPE and develop a novel photoelectrochemical sensor using a laser light source based on the synthesized nanomaterial. The obtained results from CV technique revealed excellent electrochemical reduction of FZD at CCO/SPE, giving about 167% larger peak current than that of bare SPE. CuCo$_2$O$_4$ nanorods with the high crystallinity and purity; besides, the existence of multiple valence states (Co^{2+}/Co^{3+} and Cu^{2+}/Cu^{3+}) structural lattice were beneficial to conductivity. In addition, the narrow optical band gap with two band gap values makes CCO/SPE not only generating photo-induced electron–hole (e$^-$ and h$^+$) pairs but also helping to prolong the electron–hole pair recombination time under the green light illumination, significantly enhanced electrocatalytic activity, and outstanding adsorption capacity. In optimized conditions, the CCO/SPE under green laser light irradiation detected FZD in the broad concentration range from 0.25 µM to 200 µM with a low limit of detection of 0.03 µM, and a high sensitivity of 1.11 µA µM^{-1} cm^{-2} with significantly repeatability, good anti-interfering capability, long-term storage stability, and actual applicability.

Data availability

The data supporting this article have been included as part of the ESI.†

Author contributions

Conflicts of interest

The authors declare that they have no known competing financial interests or personal relationships that could have appeared to influence the work reported in this paper.

Acknowledgements

References

1 I. J. D. Priscillal and S.-F. Wang, Fergusonite-type rare earth niobates ANbO$_4$ (A= Nd, Sm, and Eu) as electrode modifiers: deep insights into A site variations towards bifunctional electrochemical sensing applications, *Nanoscale*, 2023, **15**, 8693–8705.

2 R. Nehru, C.-W. Chen and C.-D. Dong, Sonochemically synthesized rod-like bismuth phosphate and carbon black hybrid electrocatalyst for electrochemical monitoring of hazardous sulfamethazine, *J. Environ. Chem. Eng.*, 2023, **11**, 109420.

3 N. T. Anh, N. X. Dinh, N. N. Huyen, P. T. L. Huong, V. N. Phan, P. D. Thang, H. Van Tuan, T. Van Tan and A.-T. Le, Promoting electron transfer kinetics and adsorption capacity for the detection of furazolidone in real food samples by using ag-core@Fe$_3$O$_4$-shell-based electrochemical sensing platform, *J. Electrochem. Soc.*, 2023, **170**, 017510.

4 M. D. Mund, U. H. Khan, U. Tahir, B.-E.-. Mustafa and A. Fayyaz, Antimicrobial drug residues in poultry products and implications on public health: A review, *Int. J. Food Prop.*, 2017, **20**, 1433–1446.

5 A. R. Nisha, Antibiotic residues-a global health hazard, *Vet. World*, 2008, **1**, 375.

6 N. T. Anh, N. N. Huyen, N. X. Dinh, N. T. Vinh, N. Van Quy, V. D. Lam and A.-T. Le, ZnO/ZnFe$_2$O$_4$ nanocomposite-based electrochemical nanosensors for the detection of furazolidone in pork and shrimp samples: exploring the role of crystallinity, phase ratio, and heterojunction formation, *New J. Chem.*, 2022, **46**, 7090–7102.

7 N. N. Huyen, N. T. Anh, T. L. H. Phung, N. X. Dinh, N. T. Vinh, T. T. Loan, D. L. Vu and A.-T. Le, Boosting the Selective Electrochemical Signals for Simultaneous Determination of Chloramphenicol and Furazolidone in Food Samples by Using ZnFe$_2$O$_4$-Based Sensing Platform: Correlation between Analyte Molecular Structure and Electronic Property of Electrode Materials, *J. Electrochem. Soc.*, 2022, **169**, 106517.

8 R. J. McCracken, W. J. Blanch Ower, C. Rowan, M. A. McCoy and D. G. Kennedy, *Analyst*, 1995, **120**, 2347–2351.

9 X. Li, J. Hu and H. Han, Flow-injection post-chemiluminescence determination of furazolidone in animal feeds, *Am. J. Biomed. Sci.*, 2009, **1**, 260–266.

10 J. J. Laurensen and J. F. M. Nouws, Simultaneous determination of nitrofuran derivatives in various animal substrates by high-performance liquid chromatography, *J. Chromatogr. A*, 1989, **472**, 321–326.

11 L. Yan, L. Dou, T. Bu, Q. Huang, R. Wang, Q. Yang, L. Huang, J. Wang and D. Zhang, Highly sensitive furazolidone monitoring in milk by a signal amplified lateral flow assay based on magnetite nanoparticles labeled dual-probe, *Food Chem.*, 2018, **261**, 131–138.

12 B. Healy, F. Rizzuto, M. de Rose, T. Yu and C. B. Breslin, Electrochemical determination of acetaminophen at a carbon electrode modified in the presence of β-cyclodextrin: role of the activated glassy carbon and the electropolymerised β-cyclodextrin, *J. Solid State Electrochem.*, 2021, **25**, 2599–2609.

13 N. N. Huyen, N. X. Dinh, H. Van Thanh, P. D. Thang and A.-T. Le, ZnCo$_2$O$_4$ porous nanosheets-based sensing platform for ultra-sensitive detection of Pb(II) ion at sub-parts-per-trillion level in juice and beverage samples by using differential pulse anodic stripping voltammetry, *J. Food Compos. Anal.*, 2024, **134**, 106493.

14 N. N. Huyen, L. M. Tung, T. A. Nguyen, T. L. Huong Phung, P. D. Thang, N. T. Vinh, Q. Van Nguyen, T. K. Oanh Vu, V. D. Lam, V. K. Le, N. X. Dinh and A.-T. Le, Insights into the Effect of Cation Distribution at Tetrahedral Sites in ZnCo$_2$O$_4$ Spinel Nanostructures on the Charge Transfer Ability and Electrocatalytic Activity toward Ultrasensitive Detection of Carbaryl Pesticide in Fruit and Vegetable Samples, *J. Phys. Chem. C*, 2023, **127**, 12262–12275.

15 N. Baig, M. Sajid and T. A. Saleh, Recent trends in nanomaterial-modified electrodes for electroanalytical applications, *TrAC, Trends Anal. Chem.*, 2019, **111**, 47–61.

16 F. D. S. Santos, L. V. da Silva, P. V. S. Campos, C. de Medeiros Strunkis, C. M. G. Ribeiro and M. O. Salles, Recent advances of electrochemical techniques in food, energy, environment, and forensic applications, *ECS Sens. Plus*, 2022, **1**, 013603.

17 L. Zhang, X. Zhao, W. Ma, M. Wu, N. Qian and W. Lu, Novel three-dimensional Co$_3$O$_4$ dendritic superstructures: hydrothermal synthesis, formation mechanism and magnetic properties, *CrystEngComm*, 2013, **15**, 1389–1396.

18 P. Salarizadeh, M. B. Askari, M. Seifi, S. M. Rozati and S. S. Eisazadeh, Pristine NiCo$_2$O$_4$ nanorods loaded rGO electrode as a remarkable electrode material for

© 2025 The Author(s). Published by the Royal Society of Chemistry

asymmetric supercapacitors, *Mater. Sci. Semicond. Process.*, 2020, **114**, 105078.

19 X. D. Ngo, N. H. Nguyen, T. L. H. Phung, T. A. Nguyen, N. T. Vinh, Q. N. Van, V. H. Tran, N. P. Tuyet and A.-T. Le, Deciphering the Role of p-Type ZnCo$_2$O$_4$ Semiconductor Nanoflakes for Selective Enhancement of Voltammetric Responses Toward Redox Species System: Interfacial Electron-Transfer Kinetics and Adsorption Capacity, *J. Electrochem. Soc.*, 2024, **171**, 083508.

20 A. Ramesh, P. K. Sahu, S. Duvvuri and C. Subrahmanyam, MnCo$_2$O$_4$ Spinel Nanorods for Highly Sensitive Electrochemical Detection of Nitrite, *Inorg. Chem.*, 2024, **63**, 9941–9952.

21 S. Cai, G. Wang, M. Jiang and H. Wang, Template-free fabrication of porous CuCo$_2$O$_4$ hollow spheres and their application in lithium ion batteries, *J. Solid State Electrochem.*, 2017, **21**, 1129–1136.

22 M. Chen, X. Yang, Y. Wang, X. Zhang, N. Liang and L. Zhao, CuCo$_2$O$_4$ photocatalyst for bifunctional applications: Toxic dye degradation and antimicrobial activity, *Mater. Sci. Semicond. Process.*, 2022, **146**, 106652.

23 D. Cheng, T. Wang, G. Zhang, H. Wu and H. Mei, A novel nonenzymatic electrochemical sensor based on double-shelled CuCo$_2$O$_4$ hollow microspheres for glucose and H$_2$O$_2$, *J. Alloys Compd.*, 2020, **819**, 153014.

24 A. K. Das, N. H. Kim, S. H. Lee, Y. Sohn and J. H. Lee, Facile synthesis of CuCo$_2$O$_4$ composite octahedrons for high performance supercapacitor application, *Composites, Part B*, 2018, **150**, 269–276.

25 F. Hasanvandian, A. Shokri, M. Moradi, B. Kakavandi and S. Rahman Setayesh, Encapsulation of spinel CuCo$_2$O$_4$ hollow sphere in V$_2$O$_5$-decorated graphitic carbon nitride as high-efficiency double Z-type nanocomposite for levofloxacin photodegradation, *J. Hazard. Mater.*, 2022, **423**, 127090.

26 R. Yang, J. Ji, L. Ding, X. Yuan, L. Qu, Y. Wu and Y. Li, CRISPR-Enhanced Photocurrent Polarity Switching for Dual-lncRNA Detection Combining Deep Learning for Cancer Diagnosis, *Anal. Chem.*, 2024, **96**, 13278–13284.

27 W. Geng, G. Jiang, H. Liu, L. Xue, L. Ding, Y. Li, Y. Wu and R. Yang, A Direct-Contact Photocurrent-Direction-Switching Biosensing Platform Based on In Situ Formation of CN QDs/TiO$_2$ Nanodiscs and Double-Supported 3D DNA Walking Amplification, *Small*, 2023, **19**, 2302829.

28 E. Rubin, S.-M. Shin, Y. Chen and R. Chen, High-temperature stable refractory nanoneedles with over 99% solar absorptance, *APL Mater.*, 2019, **7**, 031101.

29 J. Pal and P. Chauhan, Study of physical properties of cobalt oxide (Co$_3$O$_4$) nanocrystals, *Mater. Charact.*, 2010, **61**, 575–579.

30 H. S. Jadhav, S. M. Pawar, A. H. Jadhav, G. M. Thorat and J. G. Seo, Hierarchical mesoporous 3D flower-like CuCo$_2$O$_4$/NF for high-performance electrochemical energy storage, *Sci. Rep.*, 2016, **6**, 31120.

31 Q. Jiang, L. Liang and D. S. Zhao, Lattice contraction and surface stress of fcc nanocrystals, *J. Phys. Chem. B*, 2001, **105**, 6275–6277.

32 M. Silambarasan, N. Padmanathan, P. S. Ramesh and D. Geetha, Spinel CuCo$_2$O$_4$ Nanoparticles: Facile One-Step Synthesis, Optical, and Electrochemical properties, *Mater. Res. Express*, 2016, **3**, 095021.

33 R. Nakhowong and R. Chueachot, Synthesis and magnetic properties of copper cobaltite (CuCo$_2$O$_4$) fibers by electrospinning, *J. Alloys Compd.*, 2017, **715**, 390–396.

34 A. K. Das, N. H. Kim, S. H. Lee, Y. Sohn and J. H. Lee, Facile synthesis of CuCo$_2$O$_4$ composite octahedrons for high performance supercapacitor application, *Composites, Part B*, 2018, **150**, 269–276.

35 S. Samanta and R. Srivastava, CuCo$_2$O$_4$ based economical electrochemical sensor for the nanomolar detection of hydrazine and metal, *J. Electroanal. Chem.*, 2016, **777**, 48–57.

36 M. Haripriya, A. M. Ashok, S. Hussain and R. Sivasubramanian, Nanostructured MnCo$_2$O$_4$ as a high-performance electrode for supercapacitor application, *Ionics*, 2021, **27**, 325–337.

37 D. Guragain, C. Zequine, T. Poudel, D. Neupane, R. Gupta and S. R. Mishra, Influence of urea on the synthesis of NiCo$_2$O$_4$ nanostructure: morphological and electrochemical studies, *J. Nanosci. Nanotechnol.*, 2020, **20**, 2526–2537.

38 M. Silambarasan, N. Padmanathan, P. Ramesh and D. Geetha, Spinel CuCo$_2$O$_4$ nanoparticles: facile one-step synthesis, optical, and electrochemical properties, *Mater. Res. Express*, 2016, **3**, 095021.

39 J. Zheng, X. Liu and L. Zhang, Design of porous double-shell Cu$_2$O@CuCo$_2$O$_4$ Z-Scheme hollow microspheres with superior redox property for synergistic photocatalytic degradation of multi-pollutants, *Chem. Eng. J.*, 2020, **389**, 124339.

40 N. M. Farag, M. A. Deyab, A. M. El-naggar, A. M. Aldhafiri, M. B. Mohamed and Z. K. Heiba, Exploring the functional properties of CuCo$_2$O$_4$/CuS nanocomposite as improved material for supercapacitor electrode, *J. Mater. Res. Technol.*, 2021, **10**, 1415–1426.

41 B. Dutta, E. Kar, N. Bose and S. Mukherjee, Significant enhancement of the electroactive β-phase of PVDF by incorporating hydrothermally synthesized copper oxide nanoparticles, *RSC Adv.*, 2015, **5**, 105422–105434.

42 Z. K. Heiba, N. M. Farag, A. El-naggar, J. R. Plaisier, A. Aldhafiri and M. B. Mohamed, Influence of Cr and Fe doping on the structure, magnetic and optical properties of nano CuCo$_2$O$_4$, *Ceram. Int.*, 2021, **47**, 7888–7897.

43 H.-Y. Chen and J.-H. Chen, Preparation of p-type CuCo$_2$O$_4$ thin films by sol-gel processing, *Mater. Lett.*, 2016, **188**, 63–65.

44 T. Kokulnathan, T. S. K. Sharma, S.-M. Chen, T.-W. Chen and B. Dinesh, Ex-situ decoration of graphene oxide with palladium nanoparticles for the highly sensitive and selective electrochemical determination of chloramphenicol in food and biological samples, *J. Taiwan Inst. Chem. Eng.*, 2018, **89**, 26–38.

45 A. Sangili, V. Vinothkumar, S.-M. Chen, P. Veerakumar and K.-C. Lin, Gold nanoparticle embedded on a reduced graphene oxide/polypyrrole nanocomposite: voltammetric

sensing of furazolidone and flutamide, *Langmuir*, 2020, **36**, 13949–13962.

46 A. Roy, A. Ray, S. Saha, M. Ghosh, T. Das, M. Nandi, G. Lal and S. Das, Influence of electrochemical active surface area on the oxygen evolution reaction and energy storage performance of MnO_2-multiwalled carbon nanotube composite, *Int. J. Energy Res.*, 2021, **45**, 16908–16921.

47 Y. Liang, H. Wang, J. Zhou, Y. Li, J. Wang, T. Regier and H. Dai, Covalent hybrid of spinel manganese–cobalt oxide and graphene as advanced oxygen reduction electrocatalysts, *J. Am. Chem. Soc.*, 2012, **134**, 3517–3523.

48 T. J. Bandosz and C. O. Ania, Origin and perspectives of the photochemical activity of nanoporous carbons, *Adv. Sci.*, 2018, **5**, 1800293.

49 D. T. N. Nga, N. L. N. Trang, V.-T. Hoang, X.-D. Ngo, P. T. Nhung, D. Q. Tri, N. D. Cuong, P. A. Tuan, T. Q. Huy and A.-T. Le, Elucidating the roles of oxygen functional groups and defect density of electrochemically exfoliated GO on the kinetic parameters towards furazolidone detection, *RSC Adv.*, 2022, **12**, 27855–27867.

50 T. Yin, H. Li, L. Su, S. Liu, C. Yuan and D. Fu, The catalytic effect of TiO_2 nanosheets on extracellular electron transfer of Shewanella loihica PV-4, *Phys. Chem. Chem. Phys.*, 2016, **18**, 29871–29878.

51 R. Klingler and J. Kochi, Electron-transfer kinetics from cyclic voltammetry. Quantitative description of electrochemical reversibility, *J. Phys. Chem.*, 1981, **85**, 1731–1741.

52 A. J. Bard, L. R. Faulkner and H. S. White, *Electrochemical Methods: Fundamentals and Applications*, John Wiley & Sons, 2022.

53 J. Li, D. Kuang, Y. Feng, F. Zhang, Z. Xu and M. Liu, A graphene oxide-based electrochemical sensor for sensitive determination of 4-nitrophenol, *J. Hazard. Mater.*, 2012, **201**, 250–259.

54 X. Xu, Z. Liu, X. Zhang, S. Duan, S. Xu and C. Zhou, β-Cyclodextrin functionalized mesoporous silica for electrochemical selective sensor: simultaneous determination of nitrophenol isomers, *Electrochim. Acta*, 2011, **58**, 142–149.

55 T. Kokulnathan, T.-J. Wang, E. A. Kumar, V. Suvina and R. G. Balakrishna, Development of an electrochemical platform based on nanoplate-like zirconium phosphate for the detection of furazolidone, *ACS Appl. Nano Mater.*, 2020, **3**, 4522–4529.

56 D. Cheng, T. Wang, G. Zhang, H. Wu and H. Mei, A novel nonenzymatic electrochemical sensor based on double-shelled $CuCo_2O_4$ hollow microspheres for glucose and H_2O_2, *J. Alloys Compd.*, 2020, **819**, 153014.